JfM PAPERS

Free-surface channel flow around a square cylinder

Ian Eames[1],† and Tristan Robinson[2]

[1]University College London, Torrington Place, London WC1E 7JE, UK

[2]Department of Civil, Environmental and Geomatic Engineering, University College London, Gower Street, London WC1E 6BT, UK

The free-surface channel flow around a square cylinder is analysed, over a wide range of blocking ratios, using three-dimensional simulations. The state of the flow is characterised in terms of the Froude number upstream and downstream of the square cylinder. The simulations confirm the presence of the subcritical and choked states, and provide new insight into the supercritical state and band-gap through an analysis of how the momentum flux varies with Froude number along the channel. The influence of the blocking ratio on the flow state and drag force is analysed and shows the significant rise of drag in the choked regime.

Key words: computational methods, channel flow, wave–structure interactions

1. Introduction

Over the last 20 years, tsunami inundation of coastal urban areas has led to more than 200 000 deaths due to building failure and floating debris. These humanitarian disasters have led to greater efforts to improve building designs in susceptible regions through a better understanding of force loadings. The challenge of understanding tsunami inundation of urban areas is due to the free-surface flow being characterised by a long period and the geometrical complexity of buildings and obstructions. One way to meet this challenge is by studying simplified problems, such as how the free-surface interaction with a single body affects a steady channel flow. This idealised set-up can act as a conceptual building block for more complex multiple-body interactions.

The experimental observations of the steady flow past a square cylinder in a channel by Qi, Eames & Johnson (2014) showed two distinct flow states: a subcritical flow
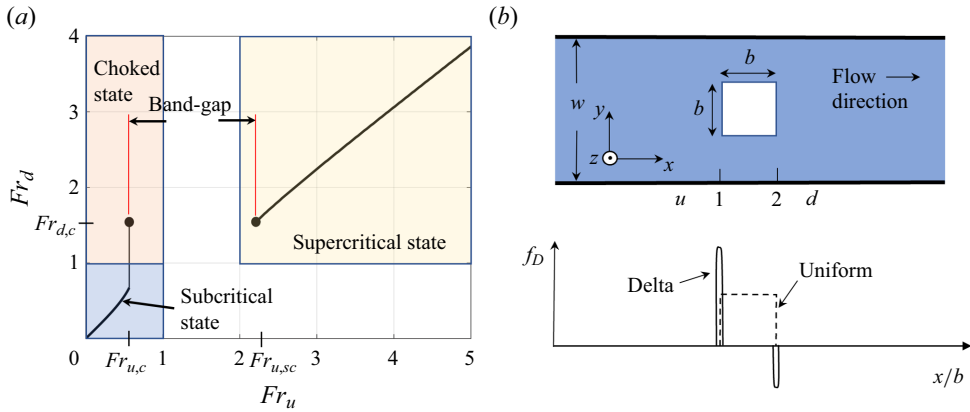
† Email address for correspondence: i.eames@ucl.ac.uk

Figure 1. (*a*) Schematic of the relationship between the Froude numbers upstream (Fr_u) and downstream (Fr_d) of an obstruction, illustrating the subcritical, supercritical and choked states; the band-gap in the Froude number is labelled. (*b*) A schematic, with notation, of the delta and uniform drag f_D representations and the coordinate axes.

state (characterised by an upstream and a downstream subcritical flow) and a choked state (characterised by a transition from a subcritical upstream flow to a supercritical downstream flow). This is represented in figure 1(*a*), and the idealised set-up is shown in figure 1(*b*), where the square cylinder is defined by a uniform section ($b \times b$) that spans the height of the channel. The square cylinder was mounted onto a rigid rod and connected to two calibrated load cells in order to infer the forces on the obstruction. In a channel of width w, this provides a section of the channel with uniform blocking ratio $\phi_B = b/w$. The experimental facilities were limited in the flow rate that could be achieved, so while the flow in the absence of the cylinder was supercritical, the presence of the cylinder caused the flow to jump to a choked state. To interpret these observations, Qi *et al.* (2014) developed a zero-dimensional model that related (in an integral sense) the loss of the momentum flux to an empirical form of the drag force. This gave a relationship between the upstream Froude number (Fr_u) and downstream Froude number (Fr_d) of the square cylinder and, together with a hydraulic jump, enabled the choked state to be analysed. At the time, the importance of the supercritical branch was not analysed or appreciated.

Motivated by a need to understand the fundamental interaction between a dam-break flow and a single building, Eames & Robinson (2022) developed a one-dimensional (1-D) model that incorporated the distinct effect of blocking and drag, caused by an obstruction, into a nonlinear shallow-water model. An analysis for steady flows identified complex critical states characterised as subcritical, choked and supercritical with a band-gap in terms of the upstream Froude number (figure 1*a*). Eames & Robinson (2022) showed that for unsteady channel flows, specifically a supercritical dam-break flow, the flow had a tendency to lock on to the steady critical flow states. Although the subcritical and choked states have been reported previously, there has been no other direct support for a band-gap in the flow state – a range of Fr_u for which no steady solution exists – except for an inference made from the supercritical experimental data of Ducrocq *et al.* (2017). Although this range matches the predictions by Eames & Robinson (2022), the supercritical branch remains unstudied. The importance of this supercritical branch is underlined by the fact that most inundation flows, created by a dam-break or tsunami, are supercritical. It is therefore essential that these critical states are studied.

In this paper, a computational methodology is adopted to explore free-surface channel flows around an obstruction, with the flow properties varying from subcritical to supercritical states. A standard open-source software is used that incorporates a number of volume-of-fluid solvers that can accommodate free-surface deformation and breaking. The numerical model used in this study is described in § 2. The results for a blocking ratio of $\phi_B = 0.2$ are first discussed in detail in § 3, covering the flow field, flow state (Fr_u, Fr_d), pressure field and total force. The general influence of the blocking ratio is discussed in § 4, before conclusions are drawn in § 5.

2. Mathematical model

The problem is posed simply: the uniform free-surface flow past a square cylinder ($b \times b$ plan), fixed in a channel (of width w) and spanning the channel height, is considered (figure 1b). The blocking ratio ϕ_B is defined to be b/w. The flow in the computational domain is initialised with a uniform horizontal flow u_0 and water height h_0 (set at $h_0 = 0.1$ m), giving an initial Froude number of $Fr_0 = u_0/\sqrt{gh_0}$ and a Reynolds number of $Re = u_0 h_0/\nu \simeq 10^4$–$10^5$.

The three-dimensional (3-D) viscous flow simulations were chosen to match closely the experimental study of Qi *et al.* (2014). The experimental study consisted of a flow quietening section, followed by a 1 m straining section before meeting a 3 m long testing section flume with channel width $w = 0.5$ m and height 0.2 m. The cylinder spanned the entire height of the domain, and the front face was located 1.5 m from the inlet. For supercritical flows, the water height rose at the front of the cylinder and generated a long persistent wake pattern. For this reason, the computational domain was chosen to be longer (at 5.0 m) and taller ($H_c = 0.3$ m) to cope with high Froude numbers. Here, we focus on the flow developed after running for a period of at least 20 s.

2.1. *Computational model*

Free-surface overturning was anticipated, which meant choosing a computational model that can cope with changes in surface topology. A standard model that can account for this effect is the volume-of-fluid formulation (Hirt & Nichols 1981) based on describing the phase as a colour function (α) that takes value 0 for a gas and 1 for a liquid. The fluid properties (e.g. density, viscosity) are described using a scalar α that represents the fraction of liquid present in a computational cell. The fluid properties are defined to vary linearly between $\alpha = 0$ and $\alpha = 1$, e.g. $P = \alpha P_f + (1 - \alpha)P_g$, where P is a scalar property, such as density (ρ) or viscosity (μ), that takes value P_g in the gas and P_f in the liquid. The momentum equation, describing the relationship between the evolution of the velocity field u_i and pressure p, is

$$\frac{\partial u_i}{\partial x_i} = 0, \quad \frac{\partial}{\partial t}(\rho u_i) + \frac{\partial}{\partial x_j}(\rho u_i u_j) = -\frac{\partial p}{\partial x_i} + \frac{\partial}{\partial x_j}(2(\mu + \mu_t)S_{ij}) + \rho g_j + \sigma \kappa \frac{\partial \alpha}{\partial x_i},$$

$$(2.1a,b)$$

where $S_{ij} = (\partial u_i/\partial x_j + \partial u_j/\partial x_i)/2$ is the mean strain rate tensor and g_j is the gravitational acceleration. The surface tension is σ, and κ is the curvature at the interface between air and water. To reduce the influence of numerical diffusion, an interface compression

scheme sharpens the gradients of the liquid–gas interface through

$$\frac{\partial \alpha}{\partial t} + \frac{\partial}{\partial x_j}(\alpha u_j) + \frac{\partial}{\partial x_j}(\alpha(1-\alpha)u_j^r) = 0, \tag{2.2}$$

where $\boldsymbol{u}^r = \nabla\alpha/|\nabla\alpha|$.

To accommodate the high Reynolds numbers, a turbulence closure is necessary to pick up the additional subgrid-scale processes. Of the many available numerical models, we choose the k–ω turbulence model (Menter 1994), which is generally better with lower Reynolds numbers adjacent to walls. This model is based on describing the evolution of the kinetic energy k and the rate of dissipation ω through

$$\frac{\partial}{\partial t}(\rho k) + \frac{\partial}{\partial x_j}(\rho u_j k) = \frac{\partial}{\partial x_j}\left((\mu + \mu_t \sigma_k)\frac{\partial k}{\partial x_j}\right) + G - \beta^* \rho\omega k, \tag{2.3}$$

$$\frac{\partial}{\partial t}(\rho\omega) + \frac{\partial}{\partial x_j}(\rho u_j \omega) = \frac{\partial}{\partial x_j}\left((\mu + \mu_t \sigma_\omega)\frac{\partial\omega}{\partial x_j}\right) + \frac{\gamma G}{v_t} - \beta\rho\omega^2 + 2\rho(1-F_1)\frac{\sigma_{\omega 2}}{\omega}\frac{\partial k}{\partial x_j}\frac{\partial\omega}{\partial x_j}, \tag{2.4}$$

where

$$G = \tau_{ij}\frac{\partial u_i}{\partial x_j}, \quad \mu_t = \frac{\rho a_1 k}{\max(a_1\omega, SF_2)}. \tag{2.5a,b}$$

The coefficients a_1, c_1 and β^* and blending functions F_1 and F_2 are described by Menter (1994).

The computational model is solved using OpenFOAM's interFoam module with the waves2Foam package (Jacobsen, Fuhrman & Fredsoe 2012) so that the non-reflecting inlet and outlet boundary conditions can be imposed. The turbulence closure model was set to be the default k–ω turbulence model. The non-reflecting inlet condition was applied on the first 0.5 m of the computational domain, while the outlet constraint was applied on the last 0.5 m of the domain. No-slip conditions were applied on the channel and cylinder walls, and on the surface $z = 0$. On the upper surface of the computational domain, the static pressure is set to a constant and a slip condition is applied. A weak turbulent intensity of 0.037 m s^{-1} is applied on the inlet condition. The sensitivity of any results to a turbulence closure model depends on the range of *Re* and the geometry. This is especially true for flow past circular cylinders, where the point of separation can shift dramatically. For flows past buildings with sharp corners, the drag force shows less sensitivity to the turbulence modelling.

The numerical results were compared against a 1-D shallow-water model based on describing the influence of the cylinder on the flow as being through a distributed drag and blocking (see Eames & Robinson 2022). The relationship between upstream and downstream Froude numbers can be calculated from the steady-state solution (see § 3.1). The relationship between the initial and final states required solving the unsteady shallow-water model until a steady solution was achieved.

2.2. *Diagnostic tools*

The mean flow was orientated along the x-axis, with the y-axis being directed across the channel. The main diagnostic was the local Froude number, defined as a function of x and y and evaluated as $Fr(x) = \bar{u}/\sqrt{g\bar{h}}$ from the depth-averaged speed $\bar{u} = (1/\bar{h})\int_0^{H_c} u(x, y, z)\,\alpha\,\mathrm{d}z$ and height $\bar{h} = \int_0^{H_c} \alpha\,\mathrm{d}z$. Upstream of the cylinder, the flow tends to be uniform between the quietening section and cylinder, so that Fr_u can be

identified from a single value on the centreline. The Fr_d value is obtained by averaging across the channel width. The drag force on the cylinder is defined as

$$F_D = \hat{x} \cdot \int_{S_b} (-p\boldsymbol{I} + \boldsymbol{\tau}) \cdot \hat{\boldsymbol{n}} \, \mathrm{d}S, \tag{2.6}$$

where S_b is the cross-sectional area of the channel domain and $\boldsymbol{I}$ is the identity matrix.

When the force is oscillatory, it is necessary to average F_D over time. A dimensionless drag coefficient can be defined based on either the initial reference state $C_{D0} = 2F_D/(\rho b u_0^2 h_0)$ or the final reference state $C_D = 2F_D/(\rho b u_u^2 h_u)$, based on upstream flow variables.

2.3. *Sensitivity tests*

The influence of mesh quality was studied with the structured mesh over a computational domain $5\,\mathrm{m} \times 0.5\,\mathrm{m} \times 0.3\,\mathrm{m}$; the mesh was characterised by $770 \times 150 \times 160$ points in the streamwise, cross-stream and vertical directions. The difference between Fr and F_D evaluated from 2.5 million and 15.2 million cells was less than 2 %. Some measures, such as the critical values of Fr, showed less sensitivity to the resolution except close to the choked state. The structure of the flow is described for $\phi_B = 0.2$ over the range $0 < Fr_0 \leq 3.0$, and the influence of blocking is discussed for the range $0.1 \leq \phi_B \leq 0.4$.

3. Drag and blocking

The free-surface flow past the cylinder tends to be locked onto a unique Froude number curve whose branches can be characterised in terms Fr_u and Fr_d. The essential feature of this relationship can be understood broadly by studying how the momentum flux (M) and Fr vary along the channel. Numerical interpretation offers an opportunity to analyse these effects in isolation.

3.1. *Momentum flux analysis*

The streamwise momentum flux (M) and volume flux (q) are defined in terms of integrals in the yz-plane:

$$M = \int_A (\rho u_x^2 + p) \, \mathrm{d}A, \quad q = \int_A \rho u_x \, \mathrm{d}A \Big/ \int_A \rho \, \mathrm{d}A. \tag{3.1a,b}$$

For a velocity field characterised as uniform with depth, the width-averaged Froude number Fr_l can be related to the average velocity u_l and average water height h_l across the channel through

$$Fr_l = \frac{u_l}{(gh_l)^{1/2}}. \tag{3.2}$$

Using $q = (1 - \phi)u_l h_l$ and (3.2), h_l and u_l can in turn be expressed in terms of Fr_l through

$$h_l = \frac{q^{2/3} g^{-1/3} Fr_l^{-2/3}}{(1 - \phi)^{2/3}}, \quad u_l = \frac{q^{1/3} g^{1/3} Fr_l^{2/3}}{(1 - \phi)^{1/3}}, \tag{3.3a,b}$$

where $\phi(x)$ is the blocking ratio along the flume, taking value 0 upstream and downstream of the cylinder and value ϕ_B in the region $|x| < b/2$. The momentum flux $M = \rho w(1 -$

$\phi)(u_l^2 + \frac{1}{2}gh_l)$ can be expressed in terms of Fr_l as

$$M = \frac{M_0}{(1 - \phi)^{1/3}} \left(Fr_l^{2/3} + \frac{1}{2}Fr_l^{-4/3}\right), \quad M_0 = \rho w q^{4/3} g^{1/3}. \tag{3.4}$$

The change in momentum flux along the channel depends on the resistance caused by both the channel walls and the obstruction. For a steady flow, the change in momentum flux across the obstruction is dominated by the total force on the cylinder (2.6) and described by

$$M_u - M_d = F_D. \tag{3.5}$$

For the 1-D model, the influence of resistance on the flow is expressed in terms of a distributed drag force f_D, where $\partial M/\partial x = -f_D$. Eames & Robinson (2022) treated the obstructions as a region of uniform blocking and distributed drag, with

$$f_D = \frac{1}{2}\rho C_R h u_l^2 (H(x - b/2) - H(x + b/2)), \tag{3.6}$$

where $H(\cdot)$ is the Heaviside step function and C_R is a constant dependent on the contraction under investigation.

The adjustment can be expressed as

$$M_1 = M_u, \quad M_1 - M_2 = \int_{-b/2}^{b/2} f_D \, dx, \quad M_d = M_2. \tag{3.7a–c}$$

In reality, a change in channel width has a simultaneous effect on the momentum flux and blocking. The front of a square cylinder leads to a reduction of momentum flux over a short region and a partial recovery at the rear. One way to account for this more realistic change is to represent the force on the flow as a delta function (δ) (figure 1b), reflecting the fact that there is a partial momentum flux recovery at the rear of the obstruction, so that

$$f_D = \frac{1}{2}\rho C_{R1} b u_1^2 h_1 \, \delta(x - b/2) - \frac{1}{2}\rho C_{R2} b u_2^2 h_2 \, \delta(x + b/2), \tag{3.8}$$

where C_{R1} and C_{R2} are coefficients on the front and back of the square cylinder.

The steady flow can be calculated from the jump conditions across the front and rear of the obstruction:

$$M_1 = M_u - \frac{1}{2}\rho C_{R1} b u_u^2 h_u, \quad M_2 = M_1, \quad M_d = M_2 + \frac{1}{2}\rho C_{R2} b u_2^2 h_2. \tag{3.9a–c}$$

The critical flow states can be determined by expressing M in terms of Fr_l (through (3.4)) and solving (3.7a–c) or (3.9a–c).

3.2. *Flow states*

The relationship between Fr_u and Fr_d can be determined graphically from the M–Fr_l relationship, with representative examples for distributed (3.6) and delta (3.8) resistance curves shown in figure 2(a,b), respectively. Eames & Robinson (2022) proposed that the steady flow falls into three groups (shown in figure 1a): (i) subcritical state ($Fr_u, Fr_d <$ 1), (ii) choked state ($Fr_u = Fr_{u,s} < 1$, $Fr_d = Fr_{d,s} > 1$) and (iii) supercritical state ($Fr_u (> Fr_{u,sc}), Fr_d > 1$). An important feature of the regime diagram (figure 1a) is the presence of a band-gap in Fr_u that separates the choked and supercritical states. The choked state and band-gap depend on the blocking ratio and obstacle geometry. The delta drag description incorporates both the action of drag and blocking at the same place, mimicking more closely processes that occur in a real flow, where the momentum flux and Froude number change simultaneously across the front and rear planes of the square cylinder.
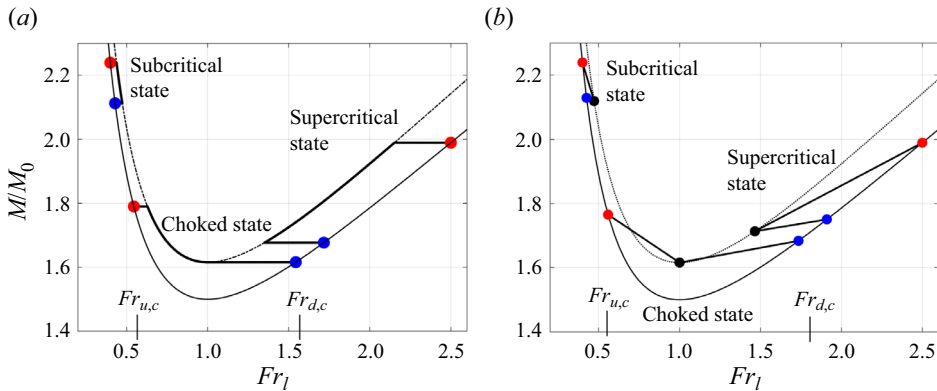
Figure 2. The relationship between momentum flux and Froude number, determined by (*a*) uniform distribution (3.7*a–c*) and (*b*) delta function (3.9*a–c*), shown with illustrative values $C_{R1} = 2.2$, $C_{R2} = 0.2$ and $C_R = 2.0$.

4. Numerical results

4.1. *Free-surface profile*

Figure 3 shows the free-surface elevation for $Fr_0 = 0.5$, 1.5 and 2.5. For a subcritical flow ($Fr_0 < 1$), the change in the water depth between upstream and downstream of the square cylinder is small, with the water flowing around its sides, and a series of standing waves is generated whose amplitude decreases downstream. For a choked flow ($Fr_0 = 1.5$), the upstream water height rises, and the downstream surface is characterised by a series of large oblique reflected waves. For a supercritical flow ($Fr_0 = 2.5$), the water begins to pile up around the front of the square cylinder, and a large rooster tail wake is created downstream. The results for figure 3(*a,b*) are consistent with the observations of Qi *et al.* (2014), while figure 3(*c*) is consistent with Riviere *et al.* (2017).

Figure 4(*a,b*) show the variation of M and Fr_l with distance along the channel. The momentum flux exhibits a finite decrease across the square cylinder as a consequence of the drag force (2.2) that acts on the obstruction, along with an associated jump in Fr_l, due to a change in the blocking ratio. The value of M decreases across the upstream face of the obstruction and shows a partial recovery across the downstream face. The variation of M with Fr_l is shown in figure 4(*c*), where the paths upstream and downstream of the obstacle are colour coded; the choked state and band-gap are indicated.

4.2. *Flow state*

Figure 5(*a*) shows a scatter plot of Fr_u and Fr_d against Fr_0. The flow states are distinguished by Fr_0 and correspond to a subcritical state, a choked state where the flow transitions from subcritical to supercritical, and a supercritical state. The abrupt transition that occurs between the states is captured quite well by the numerical results, with the trend for Fr_u collapsing onto the red curve. The 1-D model is based on local interaction and predicts the possibility of a hydraulic jump occurring in the range $|x| < b/2$ for the supercritical range; while the range is predicted, the 1-D model predicts a supercritical to critical transition that occurs within the span of the blocking–drag region and then a jump to a critical state as the flow expands. Since real flow transitions do not occur instantaneously but extend over several obstacle diameters, this unphysical transition is
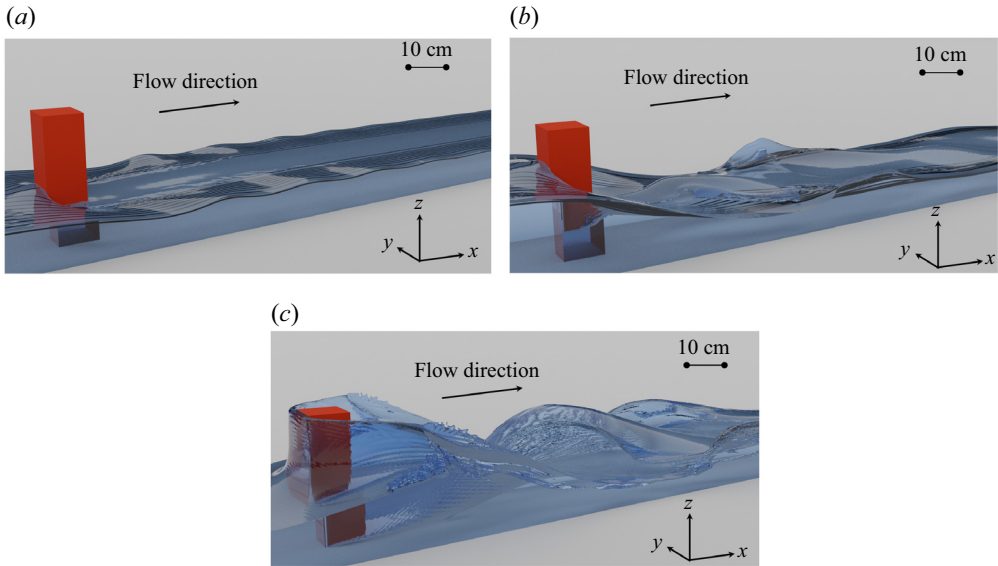
Figure 3. The free-surface flow for (*a*) $Fr_0 = 0.5$, (*b*) $Fr_0 = 1.5$ and (*c*) $Fr_0 = 2.5$. The numerical results are visualised using Blender (www.blender.org).

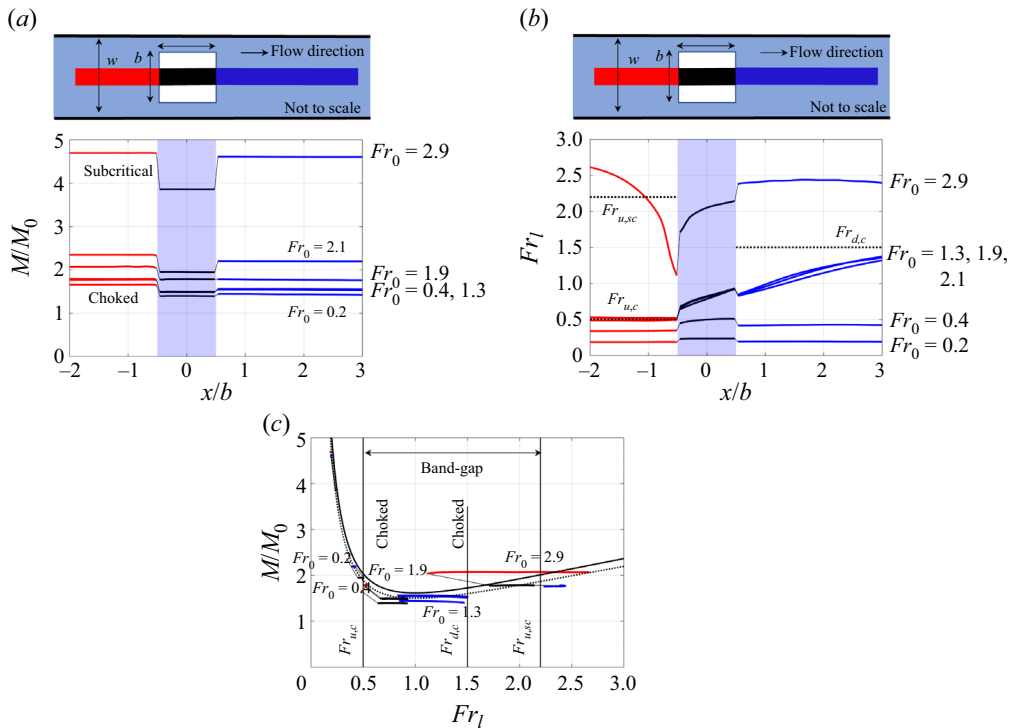Figure 4. Schematic of the channel, highlighting the three regions: upstream $x/b < -1/2$ (red), drag region $|x|/b < 1/2$ (black), and downstream $x/b > 1/2$ (blue). The variation of (*a*) M/M_0 and (*b*) Fr_l with position x/b along the channel is shown for $Fr_0 = 0.2, 0.4, 1.3, 1.9, 2.1$ and 2.9. (*c*) The variation of M/M_0 with Fr_l, for contrasting values of Fr_0.
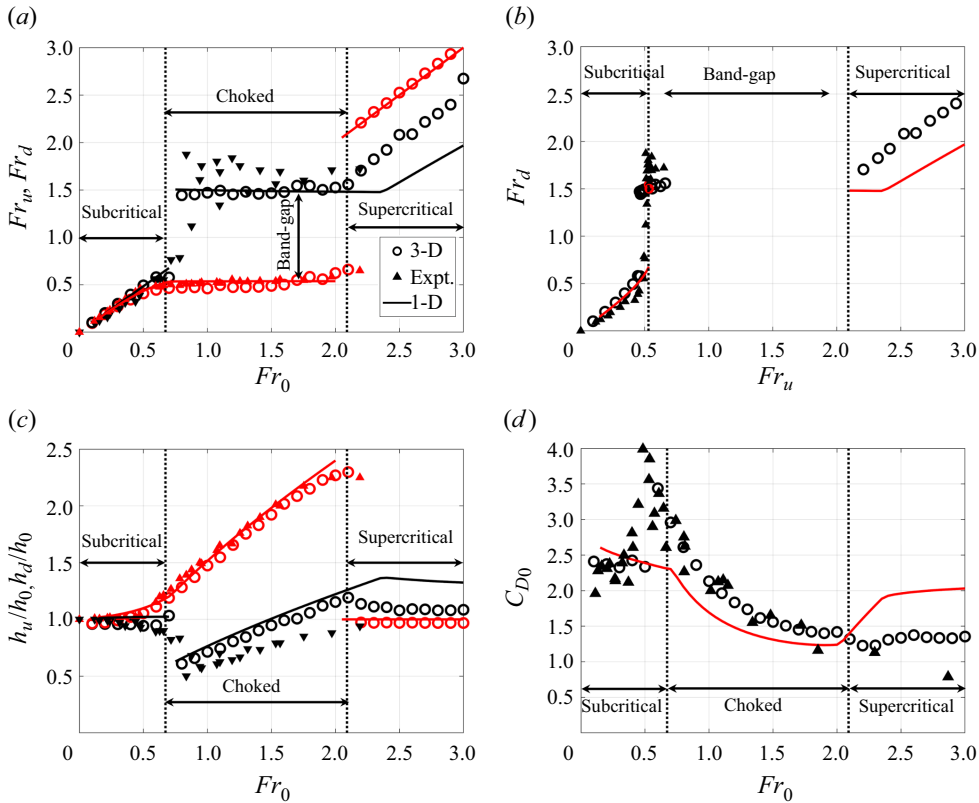
Figure 5. Comparison of the experimental (triangles, Qi *et al.* 2014), 1-D model (solid lines, Eames & Robinson 2022) and 3-D numerical simulation (circles) results. The subcritical, choked and supercritical states are indicated, along with the band-gap, in (*a,b*). In (*a,c*), red corresponds to upstream (Fr_u) and black to downstream (Fr_d) values. (*a*) The influence of the initial Froude number (Fr_0) on the upstream and downstream Froude numbers. (*b*) The data in (*a*) replotted with Fr_u versus Fr_d. (*c,d*) The variations of (upstream and downstream) water height and drag coefficient C_{D0} against Fr_0, respectively.

not observed in the numerical simulations. The numerical results show the supercritical state, and, indeed, Fr_u is higher than anticipated from the 1-D model.

Figure 5(*b*) shows a scatter plot of Fr_d versus Fr_u; for comparison, the experimental results of Qi *et al.* (2014) are plotted, along with the 1-D results of Eames & Robinson (2022). The 1-D model (red line) features a band-gap to the flow state, representing a span of Fr_u where there is no steady state. Having repeated the Qi *et al.* (2014) tests in a much longer flume, it has become apparent that the location of the flow transition, expressed generally by a hydraulic jump, moves further downstream as Fr_0 increases, meaning that while the flow transition conforms to an abrupt-change subcritical state and choked state, it appears to be continuous in the short flumes or short computational domains. The same comments apply to the transition from the choked state to the supercritical branch. The other challenge to being able to reproduce this discontinuity is simply that the bore speed decreases in magnitude, which means that the time taken to reach a steady state is much longer than the time for the drag forces to reach a steady state.

The 3-D numerical model captures the trend of the experimental results quite well. The absence of the flow regime case B2 described by Eames & Robinson (2022) from the 3-D simulations is not surprising since its occurrence is based on the instantaneous adjustment
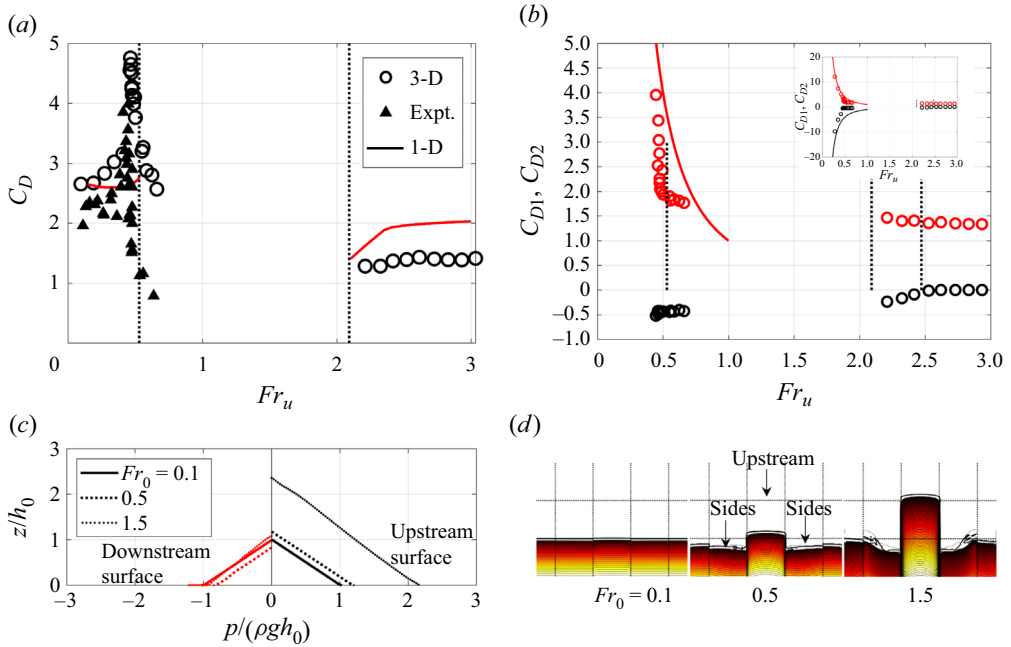
Figure 6. (*a*) The drag coefficient C_D is plotted as a function of Fr_u, and the results from the 3-D simulations are compared with experiments and the 1-D model. (*b*) The drag coefficients associated with the front and back of the cylinder (C_{D1} and C_{D2}, respectively) are compared. The inset shows the results plotted on a larger range that corresponds to low Fr_u, with the lines corresponding to the prediction $C_{Di} \sim 1/Fr_u^2$. (*c*) The instantaneous pressure distribution on the upstream and downstream centreline of the cylinder. (*d*) The instantaneous pressure distribution over the whole cylinder surface is shown for $Fr_0 = 0.1$, 0.5 and 1.5; the upstream and sides are indicated.

from a supercritical to a subcritical state within the blocking–drag region. The critical states are due largely to the blocking and drag, and since the 1-D model uses an empirical closure for the drag force, the agreement with the 3-D simulations is good except at high Fr_0. Here, the wake flow is a strongly 3-D flow.

4.3. *Force on the square cylinder*

In figure 5(*d*), the 3-D numerical results are compared against the 1-D model of Eames & Robinson (2022) and the experimental results of Qi *et al.* (2014). The forces are dominated by inertial effects, with viscous effects contributing less than 1 % to the total drag force. There are two main differences when compared with the 1-D model. First, C_{D0} is maximum at the choked state, which, while reflected in the experimental results (characterised by a degree of scatter), is not present in the 1-D model when the drag closure is based purely on a resistance. The limiting values of C_{D0} determined numerically are slightly smaller than the experimental results, which, given the mesh independence study, suggests that the possible role of ambient turbulence (noted by Qi *et al.* 2014) may be important. The second difference is that the drag force for the supercritical flow state is much lower than that predicted by the 1-D model. Since the drag force can be expressed in terms of Fr_u and Fr_d, this difference is attributed largely to a high Fr_d.

Figure 6(*a*) shows the variation of the drag coefficient C_D (based on the upstream flow conditions) with Fr_u and confirms the amplification of C_D at the choked state, corresponding to the maximum loss of the momentum flux. Of considerable interest is
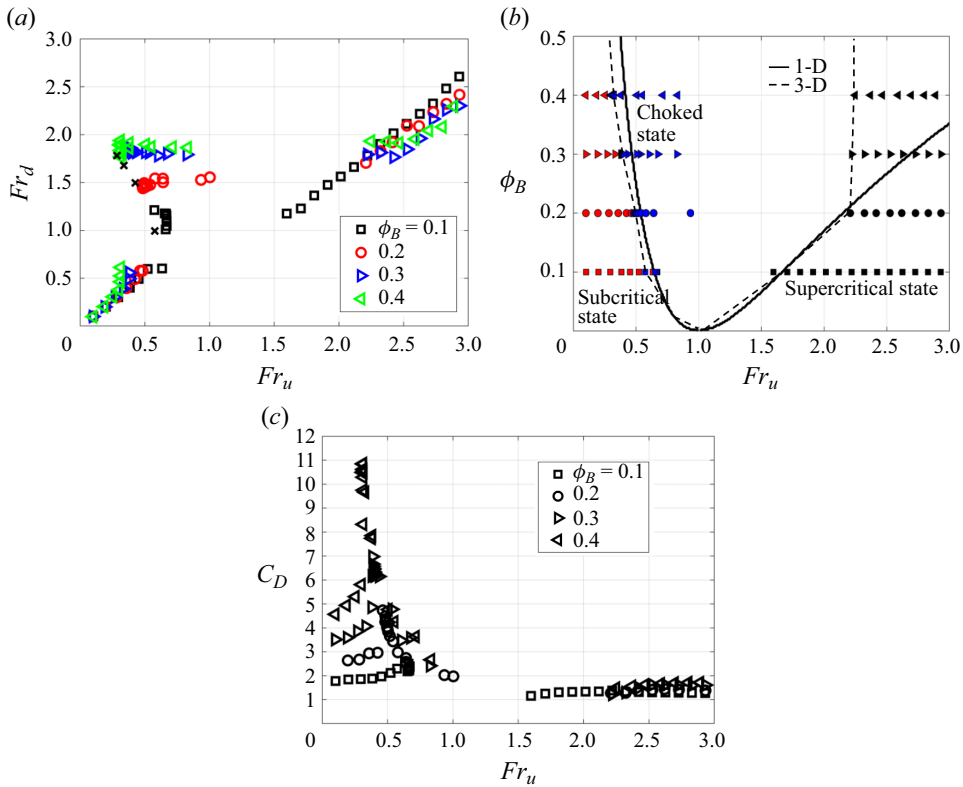
980 A16-10

Figure 7. (*a*) The influence of the blocking ratio ϕ_B over the range $0.1 \leq \phi_B \leq 0.4$ on the flow state and drag force. The $\times$ symbols represent the experimental results of Qi *et al.* (2014). (*b*) Regime diagram showing the subcritical, choked and supercritical states determined from the 3-D calculations and the 1-D model of Eames & Robinson (2022). (*c*) Variation of the drag coefficient C_D with Fr_0 for different blocking ratios.

the drag coefficient in the supercritical regime, where $C_D \sim 1.3$. It is useful to distinguish between the drag coefficient corresponding to the force on the front (C_{D1}) and back (C_{D2}) of the cylinder (figure 6*b*). The pressure field has both a hydrostatic and a dynamic component. For subcritical flows, the separate drag coefficients increase with Fr_u^{-2} since the force is dominated by a hydrostatic component with $C_{Di} \sim \frac{1}{2}gbh^2/(\frac{1}{2}bhu^2) = 1/Fr^2$; the inset of figure 6(*b*) confirms this trend. At the choked and supercritical state, C_{D1} diminishes in magnitude and C_{D2} tends to zero. For supercritical flows, we expect $F_D \sim \frac{1}{2}\rho gbh^2 = \frac{1}{2}\rho bhu^2$, giving $C_{D1} \sim 1$, which is close to the value 1.3. Figure 6(*c*) shows the variation of the instantaneous pressure field on the centreline of the cylinder, confirming a linear hydrostatic variation with z. For low Fr, the hydrostatic pressure dominates over the inertial component; while the pressure appears to be uniform across the region upstream of the square cylinder (the sides of the cylinder are identified), there is a small pressure reduction towards the edge of the front face as a consequence of the flow speeding up (figure 6*d*). Although the shape of the isobaric contours changes dramatically with Fr_0, the drag coefficient C_D is normalised by the upstream flow properties, so its variation is less dramatic, taking the values $C_D = 2.67$, 3.15 and 3.99 for $Fr_0 = 0.1$, 0.5 and 1.5, respectively.

4.4. *Influence of blocking ratio ($0.1 \leq \phi_B \leq 0.4$)*

The blocking ratio caused by the cylinder has two dramatic effects on the flow: it tends to increase the flow speed at the side of the cylinder, forcing it to achieve a critical state at a lower Fr_u, and it increases significantly the drag on the flow.

Figure 7(*a*) shows the variation of Fr_d with Fr_u for different blocking ratios. Contrasting with Qi *et al.* (2014), the new element is the supercritical flow regime and associated band-gap in Fr_u. More meaningful is the regime diagram figure 7(*b*) that distinguishes between different flow states, where the subcritical flow states are shown in red, the supercritical flow states in black, and the choked flow in blue. The blocking ratio greatly reduces the critical Fr_u when the flow becomes choked, and increases the span across which the flow must jump from the choked state to the supercritical transition. The variation of the drag coefficient C_D with Fr_0 is shown in figure 7(*c*). For low Fr_0, the influence of flow confinement on the drag coefficient is significant, even with small blocking ratios. However, for high Fr_0, the drag coefficient is weakly dependent on the blocking ratio because the bow shock tends to interact with the channel walls downstream of the cylinder.

5. Conclusion

The free-surface channel flow past a rigid body displays a remarkable degree of complexity, as characterised by the different flow states. A new detailed analysis of the flow states has been presented over a range of Fr_0 spanning subcritical, choked and supercritical states. The computational analysis has confirmed the presence of a range of Fr_u where a steady solution is not present and given insight into the supercritical branch, which was unstudied previously.

There is some initial indication by Eames & Robinson (2022) that the free-surface channel flows past an obstruction (formed, for instance, by a dam-break release) locks on to a locus of points that follows the Fr_u–Fr_d trajectory (shown in figure 3*b*) linking the supercritical state to the choked state. This underlines the significance of the present study in validating the presence of the multiple flow states and their use in characterising the types of flows that can occur.

Declaration of interests. The authors report no conflict of interest.

Author ORCIDs.

Ian Eames https://orcid.org/0000-0002-1300-5738;

Tristan Robinson https://orcid.org/0000-0002-1193-8278.

REFERENCES

DUCROCQ, T., CASSAN, L., CHORDA, J. & ROUX, H. 2017 Flow and drag force around a free surface piercing cylinder for environmental applications. *Environ. Fluid Mech.* **17** (4), 629–645.

EAMES, I. & ROBINSON, T. 2022 Horizontal dam-break flow past a blocking-drag region. *Phys. Fluids* **34**, 052104.

HIRT, C.W. & NICHOLS, B.D. 1981 Volume of fluid (VOF) method for the dynamics of free boundaries. *J. Comput. Phys.* **39**, 201–225.

JACOBSEN, N.G., FUHRMAN, D.R. & FREDSOE, J. 2012 A wave generation toolbox for the open-source CFD library: OpenFoam. *Intl J. Numer. Meth. Fluids* **70** (9), 1073–1088.

MENTER, F.R. 1994 Two-equation eddy-viscosity turbulence models for engineering applications. *AIAA J.* **32**, 1598–1605.

QI, Z.X., EAMES, I. & JOHNSON, E.R. 2014 Force acting on a square cylinder fixed in a free-surface channel flow. *J. Fluid Mech.* **756**, 716–727.

RIVIERE, N., VOUAILLAT, G., LAUNAY, G. & MIGNOT, E. 2017 Emerging obstacles in supercritical open-channel flows: detached hydraulic jump versus wall-jet-like bow wave. *ASCE J. Hydraul. Engng* **143**, 04017011.